Available online at www.sciencedirect.com
SCIENCE DIRECT
Polymer 46 (2005) 3871–3883
polymer
www.elsevier.com/locate/polymer

Poly[styrene-*b*-*maleated* (ethylene/butylene)-*b*-styrene] (mSEBS) block copolymers and mSEBS/inorganic nanocomposites: I. Morphology and FTIR characterization

Tety Kwee[a], K.A. Mauritz[a,*], F.L. Beyer[b]

[a]*Department of Polymer Science, The University of Southern Mississippi, Southern Station Box 10076, Hattiesburg, MS 39406-0076, USA*
[b]*Multifunctional Materials Branch, Weapons and Materials Research Directorate, Army Research Laboratory, Aberdeen Proving Grounds, MD 21005-5069, USA*

Received 24 September 2004; received in revised form 2 January 2005; accepted 10 February 2005
Available online 7 April 2005

Abstract

Self-assembled, [block copolymer]/[pure silicate and ORMOSIL] nanocomposites were created via sol–gel processes for silicate and organically-modified silicate (ORMOSIL) monomers in the presence of sulfonated *maleated* poly(styrene-*b*-ethylene/butylene-*b*-styrene) (mSEBS). Microscopic and small angle X-ray scattering (SAXS) studies showed that unmodified mSEBS has hexagonal packed PS cylinder morphology, but sulfonation causes the morphologies to be frustrated. The morphology of pure silicate nanoparticle-containing nanocomposites is phase separated, although further frustrated. The morphologies of the ORMOSIL-modified materials were different, less-ordered and show the influence of the nature of the organic group on self-assembly. Despite differences in morphology, degree of order, and different inter-domain spacings, all but the pure silicate-containing hybrid have the same PS domain width (25–30 nm). The dispersed nanoparticles are roughly spherical and some can grow to exceed the block copolymer domain sizes. All filled samples have inter-domain spacings, derived by SAXS analysis, that are larger than that of the corresponding unfilled sulfonated mSEBS, which reflects insertion of silicate or ORMOSIL structures. FTIR spectroscopy indicated successful Si–O–Si bond formation, which shows that the inserted particles are indeed crosslinked.

Keywords: Block copolymer/silicate; Nanocomposites; Morphology

1. Introduction

Most commercial block copolymers (BCPs) are of the ABA type, where the A blocks consist of hard segments and the B blocks are 'soft' in the sense of having a low glass transition temperature, T_g. In BCPs where A is polystyrene (PS), the equilibrium morphology can adopt a range of geometries such as PS spheres, hexagonally packed PS cylinders (HPC), and PS lamellae. The main factors determining the particular morphology, given reasonably high total molecular weight, are PS volume fraction and free energy considerations represented by the Flory–Huggins interaction parameter, χ_{S-B} for the two dissimilar blocks [1]. Additional parameters include solvent type in the case of film casting, the relative block affinity of a solvent, rate of solvent evaporation, annealing time, and annealing temperature [2–7].

In this study, unique nanostructured organic/inorganic hybrid materials based on in situ domain-targeted sol–gel reactions were created using sulfonated poly[styrene-*b*-(*maleated* ethylene-*co*-butylene)-*b*-styrene] (mSIBS) as the morphological template in the sense that the polymerizations of hydrolyzed tetraethylorthosilicate (TEOS) monomers are selectively grown within/around the sulfonated PS phase. In prior related work, a morphology shift from HPC to lamellar geometry was observed upon increasing the sulfonation level in non-maleated poly(styrene-*b*-ethylene/butylene-*b*-styrene) (SIBS) systems which was attributed to increasing χ_{S-EB} as a result of an enhancement of the polarity difference between the two dissimilar block phases [8]. As shown in Fig. 1, the polarity of the PS blocks is

* Corresponding author. Tel. +1 601 266 5595; fax: +1 601 266 5635.
E-mail address: kenneth.mauritz@usm.edu (K.A. Mauritz).

0032-3861/$ - see front matter © 2005 Elsevier Ltd. All rights reserved.
doi:10.1016/j.polymer.2005.02.076

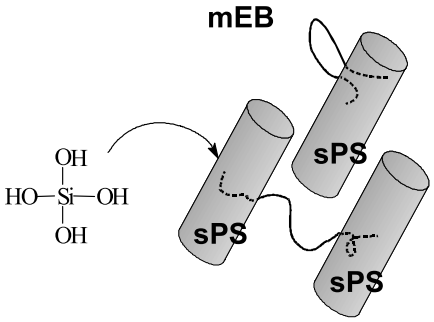

Fig. 1. Depiction of the selective migration of hydrolyzed TEOS molecules to sulfonated (s) PS domains in or around which condensation reactions between SiOH groups generate silicate nanoparticles in mSEBS.

increased through sulfonation and the working hypothesis is that polar $Si(OH)_4$ monomers preferentially migrate to the polar sPS domains forming a condensed quasi-network. The main parameters that influence sol–gel reactions and the resultant solid structure are pH, reaction temperature, reaction time, and drying conditions [9].

The focus of this paper involves creating and evaluating the morphology of unmodified and sulfonated mSEBS, as well as organic/inorganic nanostructured materials derived from in situ sol–gel reactions of TEOS and the organoalkoxysilanes phenyltriethoxysilane (PTEOS) and isobutyltrimethoxysilane (IBTMS). To this end, transmission electron microscopy (TEM) and atomic force microscopy (AFM) were utilized. The morphological information derived from microscopy was supplemented by that derived from small-angle X-ray scattering (SAXS) analysis. Finally, the molecular structures of BCP-incorporated silicate and organically modified silicate (ORMOSIL) nanoparticles were evaluated using ATR-FTIR spectroscopy.

It was thought that the morphology and properties of these self-assembled organic/inorganic nanocomposites would be influenced by the nature of the organic R groups in the trifunctional $RSi(OH)_3$ precursor molecules that undergo condensation reactions in the sol–gel process that takes place during film formation. Compared to the bulky aromatic substituent on PTEOS, the aliphatic pendant group on IBTMS is more flexible and perhaps more compatible with the rubbery center block of sulfonated mSEBS resulting in less continuous PS domains.

2. Materials

Kraton® FG 1901X (mSEBS) was supplied by Kraton® LLC. Based on the GPC analysis, this linear triblock copolymer has a molecular weight of 74,020 g/mol and PDI of 1.92. The PS outer block content is ~28 wt%. The ethylene/butylene mid-block composition was ~70 wt%, with ~2 wt% maleic anhydride grafted in this center block. TEOS, IBTMS, and PTEOS were obtained from Gelest Co. and were used without further purification. Similarly, the solvents such as dichloroethane, THF, and toluene were obtained from Aldrich and used without further purifications.

3. Experimental

3.1. Sulfonation procedure

Sulfonation reactions were carried out according to the procedure described elsewhere [8]. Approximately 12.0 g of mSEBS material was dissolved in 120 mL of dichloroethane and stirred at 50 °C under a nitrogen environment. Acetyl sulfate was used as the sulfonating reagent and it was prepared by mixing 3.8 mL of acetic acid and 1.4 mL of concentrated sulfuric acid in 19.8 mL of dichloroethane. An appropriate amount of acetyl sulfate was added to the polymer solution and stirred for 2 h. The sulfonated polymer was collected through steam stripping and the resulting polymer was dried under vacuum. The sulfonation level was determined through end point titration analysis. Approximately 0.2 g of sulfonated mSEBS was dissolved in a 80/10 (v/v) toluene/hexanol mixture, and the titration was performed at 80 °C using 0.02 M benzyltrimethylammonium hydroxide (BTMAH) in methanol to phenolphthalein endpoint. In addition, elemental analysis was also used as a complementary method to confirm the sulfonation level.

3.2. Sol–gel reactions

Approximately 4.0 g of sulfonated mSEBS was dissolved in 60 mL of THF. The nanocomposite was prepared through a direct solution casting method using a 4:1 (mol:mol) H_2O:SiOR ratio to promote complete hydrolysis and condensation reactions between SiOH groups. *n*-propanol was used as a co-solvent to improve the miscibility between water and TEOS. The multicomponent solution was allowed to react for 4 h. The resulting sol–gel-reactive solution was then cast in a Teflon pan and sealed with aluminum foil to control the rate of solvent evaporation. The film was placed in the casting oven at 60 °C for 3 d, and then annealed under vacuum at 120 °C for 4 days. The percent silicate uptake after the sol–gel reaction was evaluated thermogravimetrically using Mettler Toledo 850 TGA instrument.

3.3. Electron microscopic studies of morphology

Images of unmodified mSEBS and silicate-containing nanocomposites were obtained using a Zeiss EM 109T transmission electron microscope (TEM) utilizing a 50 keV accelerating voltage. All specimens were sectioned with a glass knife and a diamond knife using a Reichard-Jung Ultracut E microtome at −65 °C. The sections were transferred from the edge of the diamond knife to a 600 hexagonal mesh copper grid. The thickness of the sections

was approximately 40–60 nm. In the case of the composite materials, the silicate particles have sufficient electron density contrast with the polymer matrix so that staining to highlight these features is unnecessary. The silicate incorporation in the soft-hard block morphology was also probed using TEM. In this case, soft-hard block phase contrast was provided by staining sections with ruthenium tetroxide (RuO_4). The dark and the bright regions in the images correspond to the styrenic and maleated (ethylene/butylene) phases, respectively.

Tapping mode AFM was performed using a Digital Instruments Dimension 3000 Nanoscope IIIa. Phase images were produced on the basis of the difference in local viscoelastic properties, i.e. hard vs. soft block regions. Based on the type of the silicon cantilever used, the resonance frequency was ~300 kHz, and the applied scanning frequency was 2 Hz. In order to minimize artifacts, all sample surfaces were smoothed using a diamond knife prior to phase image acquisitions. The tapping mode was used to preserve the surface topography of the sample so that the results were reproducible. The bright and dark images shown in the phase images were attributed to the styrene and maleated (ethylene/butylene) phases, respectively.

3.4. Small angle X-ray scattering analysis of morphology

Small-angle X-ray scattering data were collected using a modified Anton-Paar HR-PHK camera with pinhole collimation. The incident Cu photons were generated using a Rigaku Ultrax18 rotating anode X-ray source operated at 40 kV and 60 mA. A 0.013 mm thick Ni foil was used to remove unwanted radiation, giving an effective wavelength of $\lambda = 1.542$ Å. Data were collected on a Molecular Metrology 2D multiwire detector, located approximately 65 cm from the sample position, and then azimuthally averaged for interpretation of intensity, $I(q)$, where q is the magnitude of the scattering length vector, $q = 4\pi \sin(\theta)/\lambda$ and 2θ is the scattering angle. Background spectra, including detector noise and instrumental scattering, were subtracted from the raw data and the reduced data were placed on an absolute scale using type 2 glassy carbon as a secondary standard.

3.5. FT-IR analyses of chemical microstructure

FTIR-ATR spectroscopy was used to examine intramolecular bonding structures within silicate networks. The films were clamped on top of a germanium crystal, and spectra were collected through a 9-bounce reflectance mode. All the samples that were acquired are the result of 32 scans and the background subtracted from the resulting spectra. There is the usual question as to whether FTIR-ATR spectra are representative of the bulk. Bulk (transmission) spectra for some samples were seen to exhibit the same bands as observed in corresponding ATR spectra. In earlier studies of similar systems the sol–gel reactants were made to diffuse into pre-formed films so that the concentration of silicate was greater at the surface. However, as the films reported here were cast from miscible solutions, greater chemical homogeneity is expected, although this remains to be proven.

4. Results and discussion

4.1. Sulfonated mSEBS

The TEM and AFM tapping/phase micrographs of an unmodified mSEBS film cast from THF solvent are shown in Fig. 2. The images are similar, which provides assurance that the AFM method produces a true morphology representation. Both images indicate HPC morphology. The widths of the PS cylinders, i.e. dark features on the TEM micrograph, are 25–30 nm. The structure reflected by the SAXS intensity vs. q profile for this sample, shown in Fig. 3, is consistent with the morphology seen in the microscopy images. The SAXS peaks occurred at the relative q positions of $\sqrt{3}$, $\sqrt{7}$, and 3 times the primary peak position (q^*) and this is reflective of an HPC equilibrium morphology with long-range order. Based on the position of the primary scattering peak ($q^* = 0.0234$ Å^{-1}), the average PS inter-cylinder (axis-to-axis) spacing for HPC, $D_s = (2\pi/q^*)/(0.866) = 31.1$ nm.

The relative peak intensities on the SAXS pattern should reflect the kinetic constraints operative during film formation, and therefore processing conditions. For example, Crawford et al. observed increasing peak intensity for poly(styrene-*b*-isobutylene-*b*-styrene) BCPs as the rate of solvent evaporation in film casting was reduced [10].

TEM micrographs of mSEBS having 6.0 and 9.6 mol% sulfonation are shown in Fig. 4(A) and (B), respectively. The morphology for ~6.0 mol% sulfonation consists of cylindrical PS domains that are 'frustrated' in the sense that there are some areas in which PS cylinders do not conform to a hexagonal packing mode. The widths of the PS domains taken from micrographs are 25–30 nm. The 9.6 mol% sulfonated sample shows PS rods of diameters 25–30 nm but the overall morphology is more frustrated compared to that for 6.0 mol% sulfonation. It is relevant to cite prior similar work in which a morphology shift from HPC to lamellae was observed with high sulfonation level (~14.0 mol%) in the SEBS (non maleated) system [4].

Sulfonation enhances the polarity of the PS blocks resulting in an increase of the inter-block interaction parameter, $\chi_{PS\text{-}mEB}$. In turn, this causes an increase in interfacial surface tension between the dissimilar blocks which may cause a morphology shift as there is a drive to reduce the interfacial surface area in a condition of minimum free energy [8]. Sulfonation may also cause an overall increase in effective PS block volume fraction.

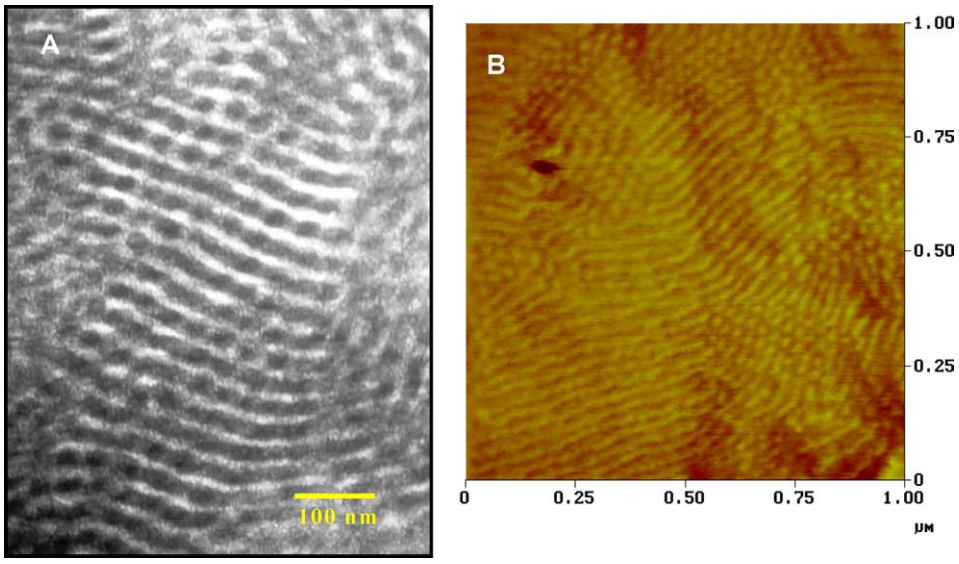

Fig. 2. (A) TEM micrograph and (B) tapping mode AFM phase image of an unmodified mSEBS sample cast from THF solvent.

Hydrogen bonding between the sulfonated PS blocks may also influence morphology.

An additional complication is posed by the fact that, during the sulfonation reaction, maleic anhydride rings in the middle block are susceptible to ring opening such that dicarboxylate groups are generated. These groups can interact with other carboxylate groups in the other chains, and this would, in theory, affect $\chi_{PS\text{-}mEB}$.

The long-range phase separated structures of sulfonated mSEBS were also probed using SAXS analysis. As seen in Figure 5, the q peaks for 6.0 mol% sulfonation are located at $\sqrt{3}$ and $\sqrt{7}$ times the position of the primary reflection peak, q^*. This sequence indicates hexagonal packed cylinder morphology to the limited degree that three peaks are visible. Based on $q^* = 0.0258$ Å^{-1}, the average PS interdomain spacing is $\sim$28.2 nm.

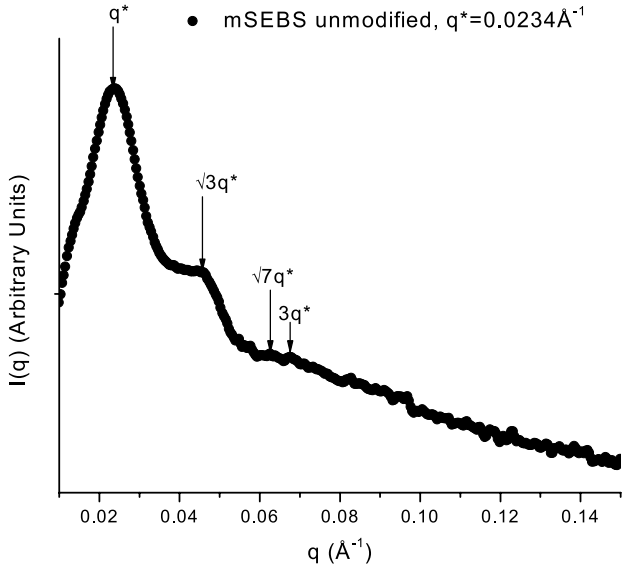

Fig. 3. SAXS intensity vs. q profile for an unmodified mSEBS film that was cast from THF solvent. The primary scattering peak is located at $q = q^* = 0.0234$ Å^{-1}.

The second reflection peak of 9.6 mol% sulfonated mSEBS at $2q^*$ seems to be more intense compared to the second peak for 6.0 mol%, perhaps suggesting less diffuse interphases for 9.6 mol% sulfonation. The peak at 2q* suggests lamellae but there are no peaks beyond this reflection; therefore, we hesitate to place this morphology into this category solely based on SAXS results and for this reason no D_s value was calculated. The TEM micrograph in Fig. 4(B) does not show lamellar morphology, but what might be described as an array of considerably disordered rods. TEM and AFM probe morphology from different perspectives and the general conclusion is that this sample is phase separated, albeit disordered. Perhaps a way of rationalizing these data is to say that this is a morphology that is intermediate between rods and lamellae.

Fingerprints of the effect of sulfonation on the mSEBS chemical structure are seen in the FTIR spectra in Fig. 6. The band assignments are largely based on the compilations of Conley [11].

The following peaks exist in the spectra of both the unsulfonated and sulfonated samples. The peak at $\sim$698 cm^{-1} is in the position for C–H out-of-plane bending for aromatic rings. There is a peak at around 1450 cm^{-1} in the position of asymmetric C–H stretching in CH_3 groups. The peak at 1603 cm^{-1} is in the vicinity of C=C stretching in aromatic rings.

In the sulfonated sample spectrum, the peak at $\sim$1060 cm^{-1} is in the vicinity of the symmetric stretching vibration in SO_3H groups and the peak at $\sim$1184 cm^{-1} is around that for the asymmetric stretching vibration in these groups. There is a band at 907 cm^{-1} for sulfonated polystyrene that corresponds to the stretching of the S–O bond with single bond character in the SO_3H groups. There is a weak band around this position in the unsulfonated

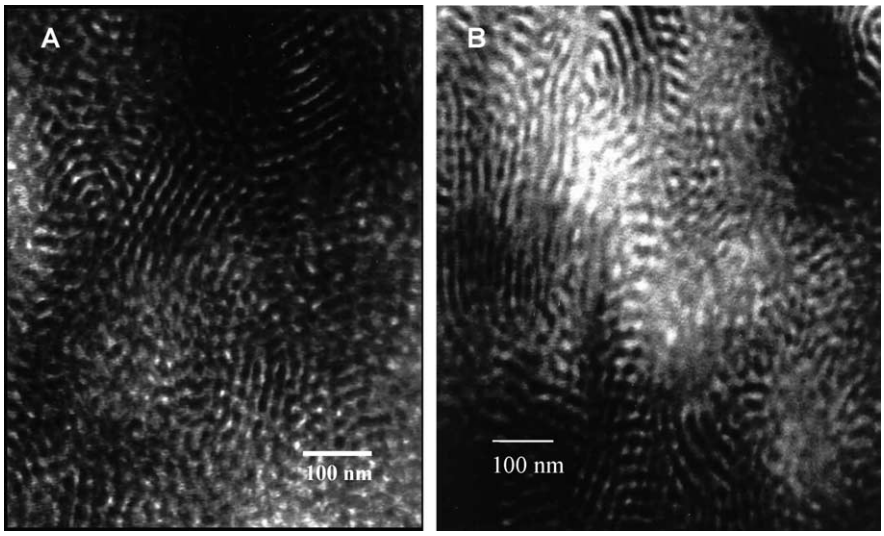

Fig. 4. TEM micrograph of sulfonated mSEBS: (A) 6.0 mol% sulfonation; (B) 9.6 mol% sulfonation.

mSEBS spectrum and a shoulder on a strong band in the sulfonated mSEBS spectrum.

The following peaks relate to the maleic anhydride rings in the center block and whether or not these rings have opened during the sulfonation reaction thereby creating dicarboxylic acid groups. The following fingerprints are useful in this regard. Anhydrides have two C=O bands due to the vibrational coupling of these groups. For example, in the case of succinic anhydride, these bands are located at 1871 cm^{-1} (asymmetric stretching) and at 1793 cm^{-1} (symmetric stretching). Inspection of the spectra in Fig. 6 shows that there are no strong bands present although there are weak absorbances at these wavenumbers. Cyclic anhydrides exhibit strong bands around 1310–1210 cm^{-1} due to C–O–C stretching vibrations and there is in fact an absorbance in this region for both the unsulfonated and sulfonated samples. As there are neither aliphatic nor aromatic groups in this polymer that would have bands in this region, it might be concluded that there are at least some anhydride rings that survive the sulfonation reaction.

Evidence of ring opening would be the presence of a band at 1765–1750 cm^{-1} for non-hydrogen bonded COOH groups and/or a band at 1720–1710 cm^{-1} for C=O stretching in COOH dimers. There is in fact a weak band at around 1765–1750 cm^{-1} for both the unsulfonated and sulfonated samples, and a band at around 1730 cm^{-1} that is strong for the unsulfonated sample but weaker for the sulfonated sample. Furthermore, there appears to be is a band at ~920 cm^{-1}

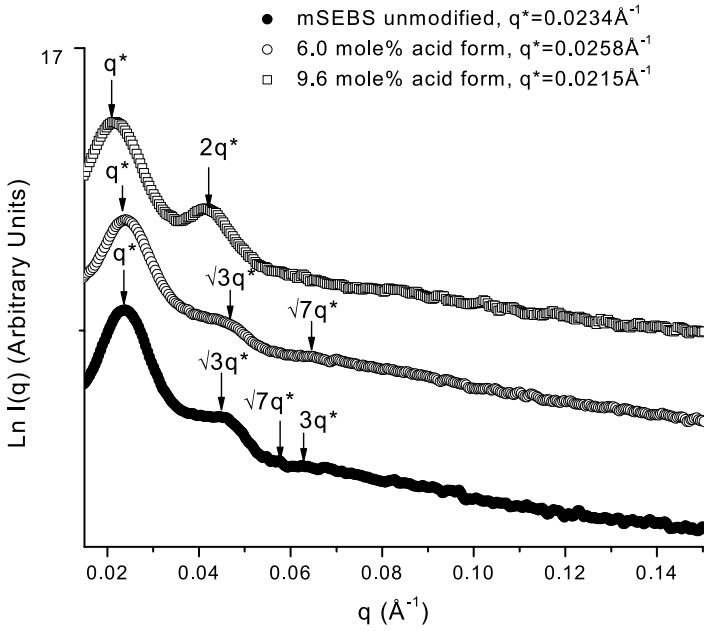

Fig. 5. SAXS intensity vs. q profiles for sulfonated mSEBS samples and an unsulfonated control sample.

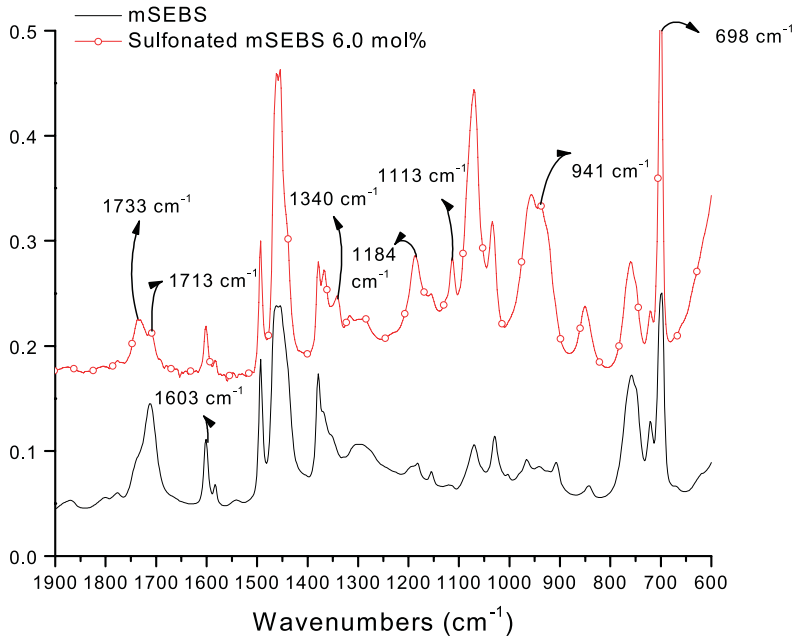

Fig. 6. FTIR/ATR spectra of unmodified mSEBS and mSEBS having 6.0 mol% sulfonation.

which is in the region of O–H out-of-plane bending in the COOH dimers. Thus, while the spectroscopic evidence is not totally understood, it is apparent that the rings are neither all open nor totally closed in either case.

4.2. Silicate-containing nanocomposites

The influence, on morphology, of having TEOS-derived silicate structures (9.5 wt% silicate) in a 6.0 mol% sulfonated mSEBS sample is seen in Fig. 7. Both the TEM and AFM tapping/phase images depict the same morphology that is clearly phase separated, although 'frustrated' in the sense of having less ordered PS cylinders in an array with a low degree of long-range order. The loss of order may be attributed to silicate quasi-networks in the form of particles that grow around the functionalized PS blocks at the same time that the morphology is evolving during film formation. These growing particles may restrict the mobility of the polymer chains during this process. The increased widths of the PS domains in the hybrid are in 30–40 nm which accounts for the inclusion of silicate structures around these domains. The interfaces also appear to be diffuse, which suggests phase mixing or intrusion of silicate fragments into the soft block domains.

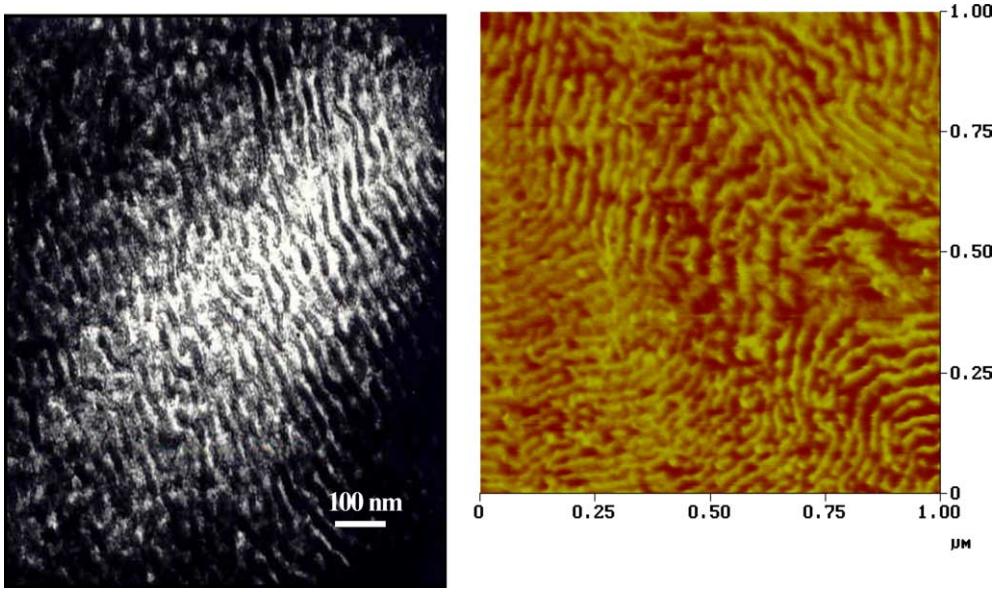

Fig. 7. (A) TEM micrograph and (B) AFM tapping mode phase image of a TEOS-modified mSEBS having 6.0 mol% sulfonation and 9.5 wt% silicate content.

The TEM micrograph of the unstained sample in Fig. 8 shows dispersed silicate particles with sizes in the range 30–50 nm, which is in the range of BCP inter-domain spacings. Thus, the inorganic inclusions in this case can indeed be classified as 'nanoparticles'. The inset in Fig. 8 indicates that the nanoparticles are approximately spherical and somewhat uniformly distributed. The bright circles surrounding some particles seem to be the result of film separation due to electron beam damage at silicate/polymer interfaces.

The low degree of long-range microstructure in the silicate containing nanocomposites as seen in the TEM and AFM images is supported by SAXS analysis based on the scattered intensity vs. q profiles in Fig. 9. The unfilled sulfonated mSEBS sample has two weak secondary peaks at positions that suggest a disordered HPC morphology while the corresponding silicate containing sample, has, at most a rather weak secondary peak. It is reasonable that silicate structures that simultaneously form around developing PS cylinders would disrupt HPC morphology. Using $q^* = 0.0164\ \text{Å}^{-1}$ for the composite, D_s is $\sim$44.2 nm if a 'loose' HPC morphology, as seen in Fig. 7, is assumed. The increase in D_s compared to that for sulfonated mSEBS suggests the inclusion of silicate structures around the PS cylinders and perhaps this would also account for the formation of diffuse phase boundaries seen in the TEM micrograph.

Signatures of silicate incorporation are also seen in the FTIR-ATR spectrum in Fig. 10. Peaks associated with *asymmetric* stretching in Si–O–Si groups in linear and cyclic fragments of silicate structures appear at 1068 and 1018 cm^{-1} and the Si–O–Si *symmetric* stretching band appears at 805 cm^{-1} [11,12]. The Si–O–Si *symmetric* stretching is theoretically inactive, but can be present if there is a considerable degree of distortion from coordinative symmetry in SiO_4 structural subunits [12]. The main conclusion based on this evidence is that bonded silicate structures have formed. The peak at 964 cm^{-1} is for the Si–OH vibration, and therefore uncondensed SiOH groups. On quantitative inspection of this spectrum, it is seen that the degree of condensation is high.

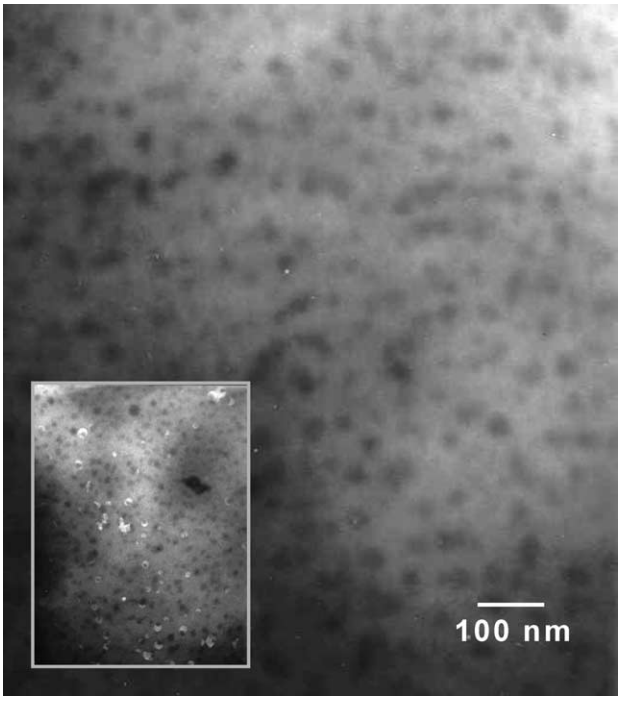

Fig. 8. TEM micrograph showing dispersed silicate particles in an mSEBS sample that has 6.0 mol% sulfonation and 9.5 wt% silicate.

4.3. Organically modified silicate-containing nanocomposites

The TEM images in Fig. 11 show the morphologies of two different nanocomposites based on in situ sol–gel processes for IBTMS and PTEOS semi-organic monomers in a 6.0 mol% sulfonated mSEBS matrix. These two materials have approximately the same weight percent uptake (19.5 and 19.1%) so that comparisons between their structures on the basis of filler composition are meaningful. From Fig. 11(A), the widths of the sPS rod domains (dark features) for IBTMS modification are 25–30 nm. The image in Fig. 11(C), for the PTEOS-modified hybrid, shows more continuous, i.e. longer, PS rods although the domain width is also 25–30 nm. Perhaps the condition of having a more extended PS phase than that in the IBTMS-modified material may be due to a greater compatibility of the aromatic pendant groups in PTEOS with the PS phase. It is speculated that the aliphatic isobutyl groups may lower interfacial surface tension so as to reduce the size of the isolated phase in a manner similar to the action of blend compatibilizer molecules.

The ORMOSIL nanoparticles of the IBTMS-derived nanocomposites, seen in the TEM micrograph for the unstained sample, in Fig. 11(B), are approximately 50–100 nm in size and appear to be dispersed and not aggregated. As seen in Fig. 11 (D), the particle sizes in the PTEOS-modified material are larger, in the approximate range 50–150 nm, and the size distribution is broader compared to that of the IBTMS-modified nanocomposite. Although the sample is unstained, light–dark striations, reflective of BCP phase separation, can be seen in Fig. 11 (D). In this way, this figure shows that at least some particles can grow to sizes larger than inter-domain spacings.

Silicate particles are also seen in the AFM tapping/phase images in Fig. 12. Here, the particles are seen as the bright spots against the phase separated morphology owing to the sharp contrast in local viscoelastic properties. In these particular images, the particles are generally not of a size that exceeds the spacing between the phase features. In Fig. 12(B), it is seen that that particles reside along the dark striations, which is the maleated EB phase. However, caution should be exercised before assigning the location of the particles to the mEB regions because the contrast

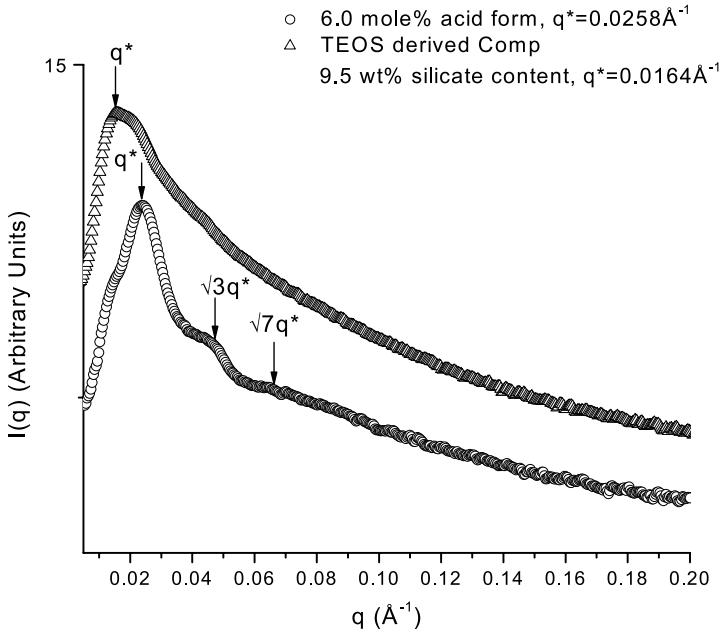

Fig. 9. SAXS intensity vs. q profiles for a 6.0 mol% sulfonated mSEBS sample and a corresponding TEOS-derived nanocomposite with 9.5 wt% silicate content.

between the particles and the hard sPS regions will be considerably less, which makes it more difficult to interrogate particle incorporation in the sPS regions in this mode. What can be said, on inspection of Fig. 12(B), is that there are some particles in the soft phase. The issue of particular phase residence of the particles will also be addressed in future studies by dynamic mechanical analysis by observing the influence of these fillers on the glass transition of the two phases. The IBTMS-derived nanocomposite in Fig. 12(A) has a morphology that is less

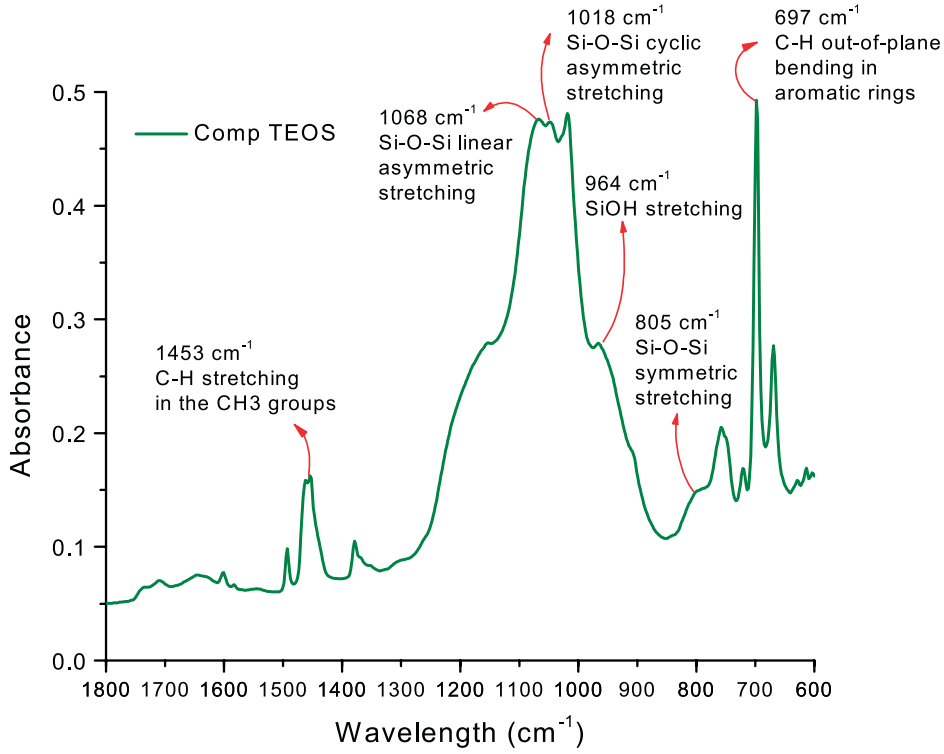

Fig. 10. FTIR-ATR spectrum of a nanocomposite that has a 9.5 wt% silicate content that was generated via an in situ sol–gel process for TEOS. Silicate bands are labeled.

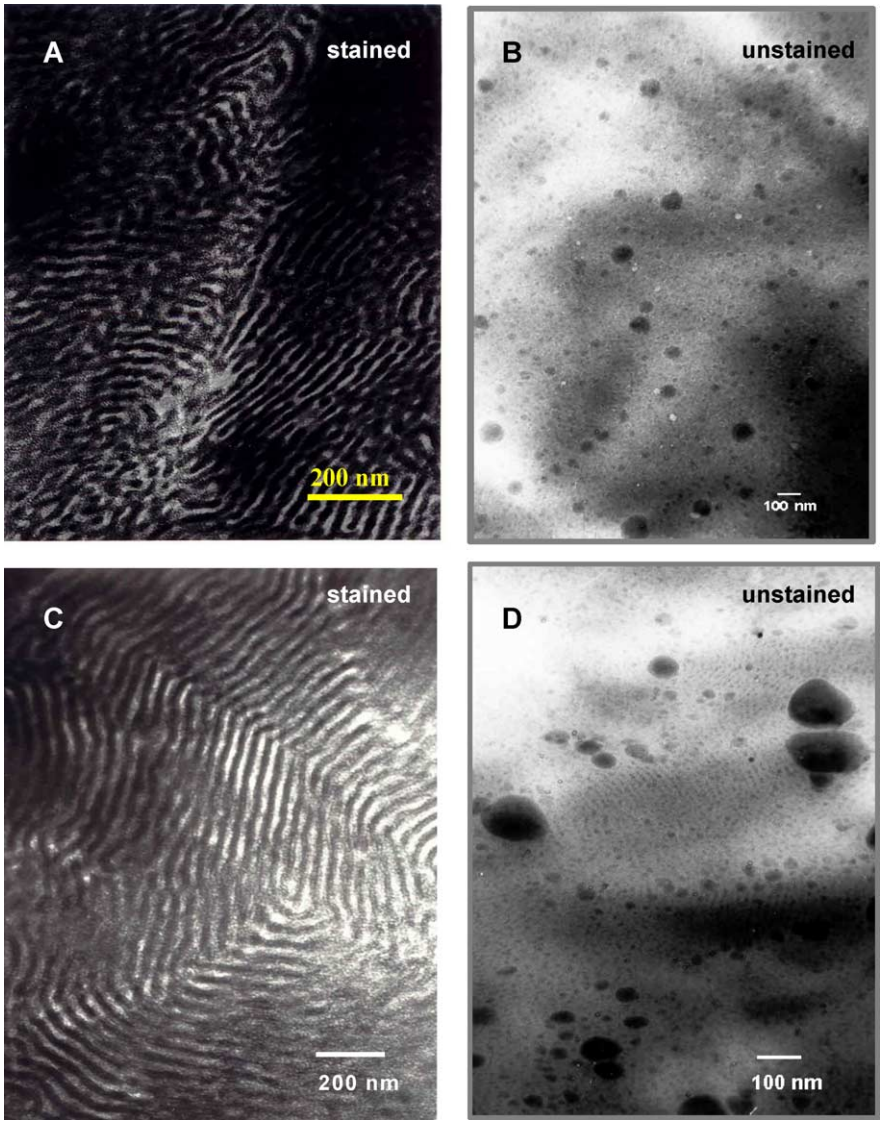

Fig. 11. TEM micrographs of stained (left) and unstained (right) nanocomposites based on 6.0 mol% sulfonated mSEBS modified with (A, B): IBTMS (19.5 wt% ORMOSIL) and (C, D): PTEOS (19.1 wt% ORMOSIL).

ordered as compared to that of the PTEOS-derived nanocomposite (B). These AFM image comparisons reflect the same relative degree of order for the two nanocomposites as seen in the respective TEM images in Fig. 11.

It might be thought that this morphology difference is due to the difference in the compatibility of the organic groups on the ORMOSIL precursor molecules for the two phases. Alkyl groups would be more compatible with the aliphatic EB phase. Aromatic rings would reasonably prefer to associate more strongly with the rings in the PS blocks, although particles are seen in the soft phase in Fig. 12(B). It is reasonable that IBTMS molecules would have greater diffusion mobility being more compatible with the major, continuous phase.

As seen in the AFM micrographs, the silicate particles are in the size range 50–150 nm, which agrees with the sizes observed via TEM. Moreover, the PTEOS-modified nanocomposite shows more continuous PS rods, which is also consistent with the TEM observation. The sizes of the silicate nanoparticles forming around the PS hard phase range from 50 to 150 nm. The phase image in Fig. 12(B) supports the results of the TEM image, which shows that the silicate particles are not as evenly distributed as compared to the situation for IBTMS, further suggesting that the majority of the bulky aromatic pendant groups in PTEOS are unable to diffuse in between the adjacent PS rods in the formation of the silicate network.

The influence of the in situ-grown ORMOSIL filler on morphology as interrogated by SAXS analysis is as follows. The lack of long-range order as seen by TEM and AFM is supported by the absence of higher order peaks in the SAXS profiles in Fig. 13. The IBTMS and PTEOS-modified samples show only two scattering peaks with the second peak located at $2q^*$ in both cases. There appears to be less

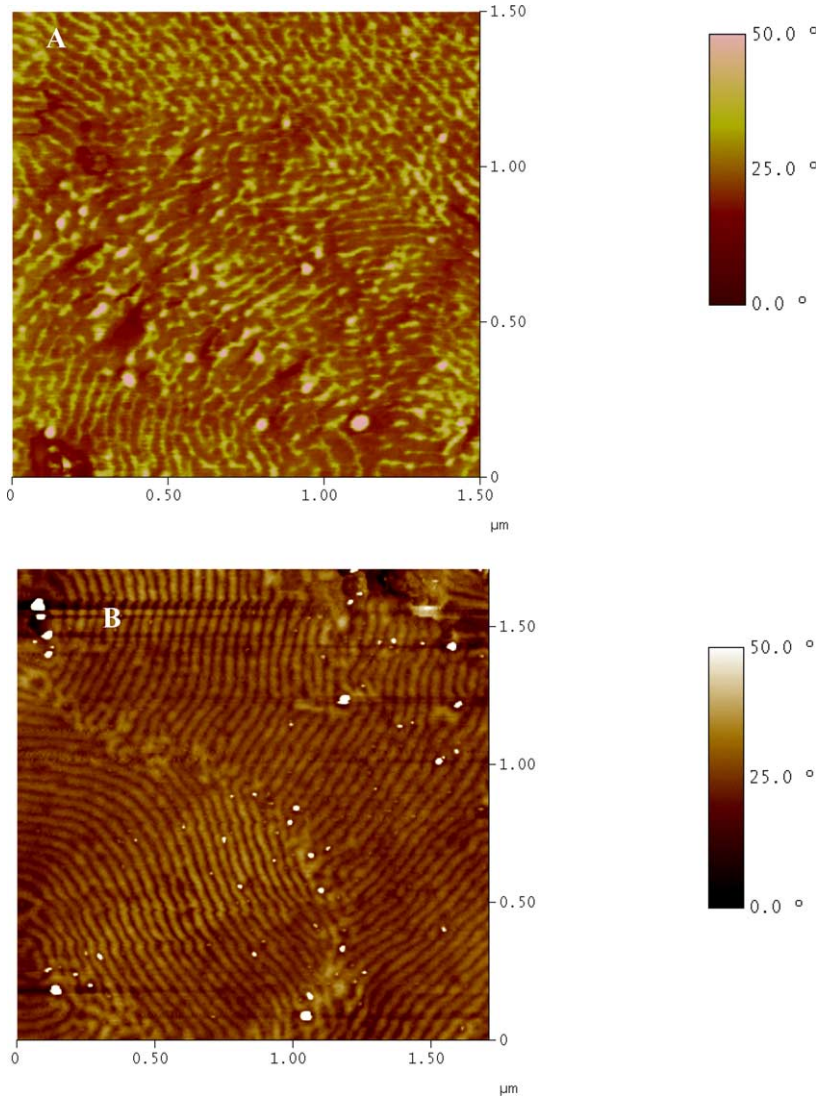

Fig. 12. AFM tapping mode phase images of 6.0 mol% sulfonated mSEBS modified by in situ sol–gel reactions of (A) IBTMS and (B) PTEOS. The images are for the same sample as in Fig. 11.

long-range order in both type of ORMOSIL-filled block copolymers than in the sulfonated but unfilled mSEBS. The primary Bragg spacing for the IBTMS sample ($2\pi/q^*$) is ~36.3 nm while that for the PTEOS-modified sample is ~28.7 nm, which is a considerable difference. The scattering data for all the samples tested are listed in Table 1. D_s for the TEOS-modified sample is significantly larger than the value for the PTEOS modification but is not much different than the value for the IBTMS modification. Nonetheless, all filled samples have inter-domain spacings that are larger than that for the corresponding unfilled 6.0 mol% sulfonated mSEBS material (~26.9 nm), which reflects the insertion of silicate or ORMOSIL structures without causing the disruption of a phase separated morphology.

The FTIR spectrum of the IBTMS-modified nanocomposite is seen in Fig. 14. The linear and cyclic Si–O–Si asymmetric stretching bands appear as components in a broad absorption envelope at 1011 and 1060 cm^{-1}. The high wavenumber shoulder on this multicomponent band is in the position for asymmetric stretching vibration in SO_3H groups. The band at 809 cm^{-1} is for Si–O–Si symmetric stretching. As before, these are fingerprints of successful condensation reactions between SiOH groups. The

Table 1
Domain sizes, from TEM, and SAXS-derived inter-domain spacings of mSEBS, sulfonated mSEBS, and nanocomposites

Sample	PS domain size (nm)	q^* ($Å^{-1}$)	D_s (nm)
mSEBS	25–30	0.0234	31.1
6.0 mol% sulfonated	25–30	0.0258	28.2
9.6 mol% sulfonated	25–30	0.0215	[a]
TEOS 9.5 wt% silicate content	30–40	0.0164	38.3
PTEOS 19.1 wt% silicate content	25–30	0.0219	28.7[b]
IBTMS 19.5 wt% silicate content	25–30	0.0173	36.3[b]

[a] Well-defined long range morphological order is present.
[b] Primary Bragg spacing.

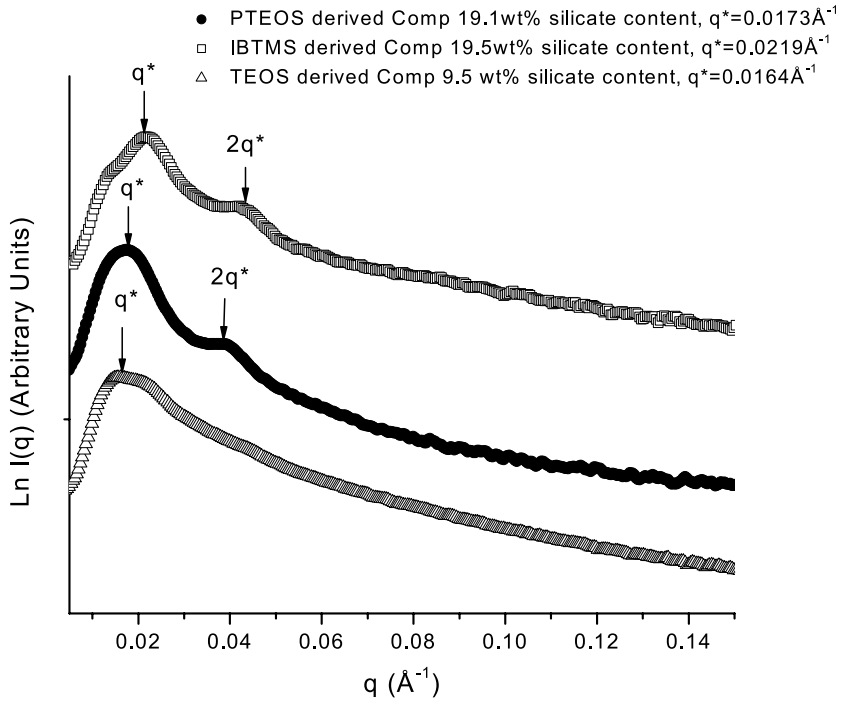

Fig. 13. SAXS intensity vs. q profiles of nanocomposites resulting from in situ sol–gel reactions of TEOS, IBTMS and PTEOS in a 6 mol% sulfonated mSEBS matrix. Filler contents and q^* values are indicated.

absorption for uncondensed SiOH groups appears as a shoulder on the 1011 cm^{-1} band at 956 cm^{-1}. In a qualitative sense, at least, the ORMOSIL component appears to possess considerable crosslinking within itself.

The band at 839 cm^{-1} can be attributed to Si–C bond stretching and the band at 1231 cm^{-1} is attributed to the CH_3 rocking vibration. The peaks at 1381 and 1368 cm^{-1} are attributed to the doublet characteristic of C–H stretching vibration in the gem dimethyl groups.

The FTIR spectrum of the PTEOS-modified nanocomposite is seen in Fig. 15. The linear and cyclic Si–O–Si asymmetric stretching bands appear on a broad absorbance

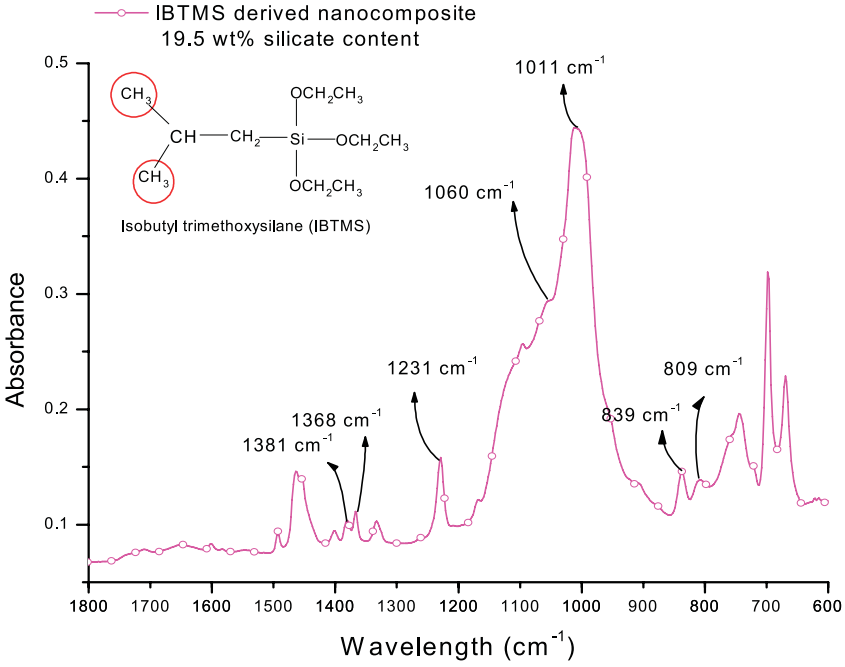

Fig. 14. ATR-FTIR spectrum of a nanocomposite resulting from in situ sol–gel reactions of IBTMS in 6.0 mol% sulfonated mSEBS. The ORMOSIL content is 19.5 wt%.

envelope at 1012 and 1055 cm^{-1} while the Si–O–Si symmetric stretching band is at 790 cm^{-1}. These, as before, are signatures of a bonded organically modified silicate structure. There is a shoulder at 960 cm^{-1} on the 1012 cm^{-1} band that could be ascribed to uncondensed SiOH groups. The sharp intense peak at 1134 cm^{-1} is associated with Si–C_6H_5 groups. The band at 1431 cm^{-1} is in the vicinity of C–C ring stretching vibration in aromatic rings that have a bonded Si atom.

5. Conclusions

Self-assembled, [block copolymer]/[pure silicate and ORMOSIL] nanocomposites were created via sol–gel processes for TEOS, IBTMS and PTEOS monomers in the presence of sulfonated *maleated* SEBS in solutions during film formation. FTIR spectra reflected the chemical modification affected by the sulfonation reaction.

TEM, AFM and SAXS studies showed that unmodified mSEBS possesses an ordered HPC morphology with PS domain sizes ~25–30 nm. Sulfonation causes morphologies that are frustrated. The morphology of pure silicate-containing nanocomposites is phase separated, although further frustrated, and this is attributed to chain mobility restrictions posed by silicate nanoparticles that grow around the sulfonated PS blocks to sizes of 30–50 nm while the BCP morphology is evolving. The morphologies of the IBTMS and PTEOS-modified materials were different and less-ordered wherein the in situ-grown particles in each case are 50–100 nm and 50–150 nm, respectively. These differences illustrate the influence of the organic group on the organo-alkoxysilane precursor monomer on self-assembly. Despite differences in morphology, degree of order and inter-domain spacings, all but the TEOS-modified variant exhibits the same PS domain width of 25–30 nm. The nanoparticles are compact, roughly spherical in most cases, can grow to exceed the domain sizes and, importantly, are dispersed and not aggregated. All filled samples have inter-domain spacings, derived by SAXS analysis, that are larger that that of the corresponding unfilled sulfonated mSEBS and this reflects an insertion of silicate or ORMOSIL structures while maintaining phase separated morphologies.

For the pure silicate and ORMOSIL-containing nanocomposites, FTIR spectroscopy showed the signatures of successful Si–O–Si bond formation, with a fraction of uncondensed SiOH groups, which shows that the inserted nanoparticles are indeed crosslinked within themselves.

Future studies will involve an evaluation of mechanical properties, including hysteresis effects and the results will be related to morphology, nanoparticle composition, and particle–matrix interactions. Dynamic mechanical analysis will probe the influence of sulfonation and nanoscopic filler composition on the glass transitions of the phases as well as phase refinement as reflected by the widths of the relaxation peaks.

Owing to the fact that these materials possess different regions that are only tens-of nanometers in extent at least in one dimension, and that these regions have sharp chemical contrast as well as functional groups, it is reasonable to consider applications involving permselective membranes and coatings. To this end, the gas and ionic transport properties of films will also be investigated in the future.

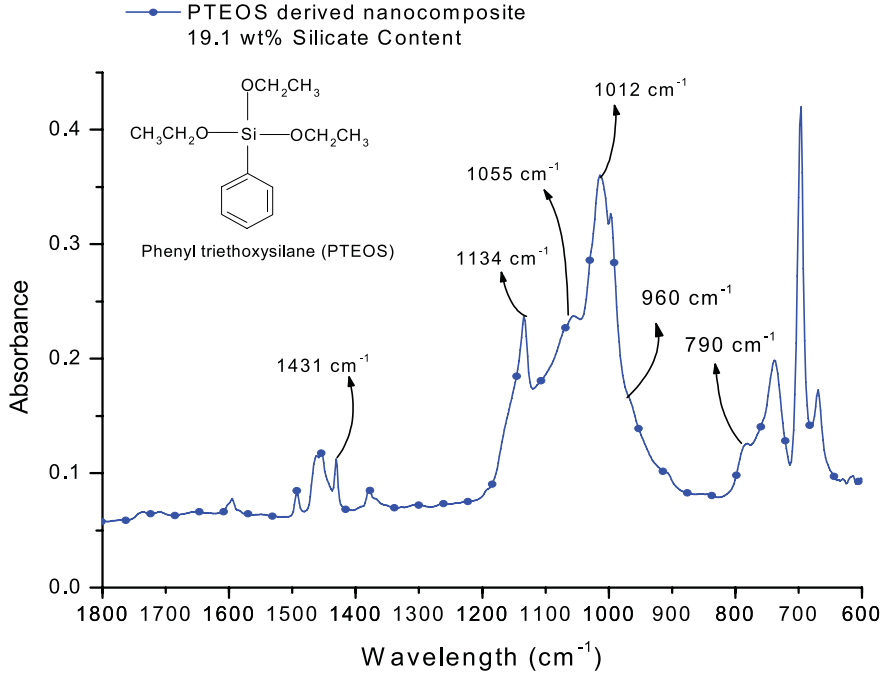

Fig. 15. ATR-FTIR spectrum of a PTEOS-modified hybrid having 19.1 wt% ORMOSIL content.

Acknowledgements

This work is supported by the DOD/EPSCoR (DAAD19-01-0498 and DAAD04-96-1-0191), and Mississippi/NSF-EPSCoR programs. The authors appreciate the donation of mSEBS samples from Kraton® LLC.

References

[1] Holden G, Legge NR, Quirk R, Schroeder HE. Thermoplastic elastomers. 2nd ed. Munich: Hanser Publications; 1996.
[2] Kim G, Libera M. Macromolecules 1998;31:2569.
[3] Funaki Y, Kumano K, Jinnai H, Yoshida H, Kimishima K, Tsutsumi K, et al. Polymer 1999;40:7147.
[4] Blackwell RI, Mauritz KA. Polymer 2004;45:3457.
[5] Quintana JR, Janez MD, Hernaez E, Garcia A, Katime I. Macromolecules 1998;31:6865.
[6] Funaki Y, Kumano K, Jinnai H, Yoshida H, Kimishima K, Tsutsumi K, et al. Polymer 1999;40:7147.
[7] Lodge TP, Hamersky MW, Hanley KJ, Huang C. Macromolecules 1997;30:6139.
[8] Mauritz KA, Blackwell RI, Beyer FL. Polymer 2004;45:3001.
[9] Brinker CJ, Scherer GW. Sol–gel science. London: Academic Press; 1990.
[10] Crawford DW, Napadensky E, Beck Tan NC, Reuschle DA, Mountz DA, Mauritz KA, et al. Thermochim Acta 2001;367:125.
[11] Conley RT. Infrared spectroscopy. 2nd ed. Boston: Allyn and Bacon; 1975.
[12] Mauritz KA, Warren RM. Macromolecules 1989;22:1730.